Astronomical Notes
Astronomische Nachrichten

Editors

K. G. Strassmeier (Potsdam/Editor-in-Chief),
G. Hasinger (Garching), R.-P. Kudritzki (Honolulu),
T. Montmerle (Grenoble), H. W. Yorke (Pasadena)

Shear-driven magnetic buoyancy oscillations

V. Vermersch[1,2] and **A. Brandenburg**[2,3,⋆]

[1] Centre de Physique Théorique, École Polytechnique, F-91128 Palaiseau cedex, France
[2] NORDITA, AlbaNova University Center, Roslagstullsbacken 23, SE 10691 Stockholm, Sweden
[3] Department of Astronomy, AlbaNova University Center, Stockholm University, SE 10691 Stockholm, Sweden

The effects of uniform horizontal shear on a stably stratified layer of gas is studied. The system is initially destabilized by a magnetically buoyant flux tube pointing in the cross-stream direction. The shear amplifies the initial field to Lundquist numbers of about 200–400, but then its value drops to about 100–300, depending on the value of the sub-adiabatic gradient. The larger values correspond to cases where the stratification is strongly stable and nearly isothermal. At the end of the runs the magnetic field is nearly axisymmetric, i.e. uniform in the streamwise direction. In view of Cowling's theorem the sustainment of the field remains a puzzle and may be due to subtle numerical effects that have not yet been identified in detail. In the final state the strength of the magnetic field decreases with height in such a way that the field is expected to be unstable. Low amplitude oscillations are seen in the vertical velocity even at late times, suggesting that they might be persistent.

1 Introduction

Dynamos convert kinetic energy into magnetic energy. A typical example is thermally driven convection. If the difference between heating and cooling across the domain is strong enough, thermal energy can be converted into kinetic energy by the Rayleigh-Bénard instability, and part of this kinetic energy can then be converted further into magnetic energy by the dynamo instability. However, if there is shear, then this can supply a major part of the kinetic energy. In view of Cowling's (1933) anti-dynamo theorem, it is clear that the magnetic field must be fully three-dimensional. This is easily achieved if the motions are three-dimensional as well. A linear shear flow is just one-dimensional, although it is in principle possible that this flow becomes nonlinearly unstable and develops fully three-dimensional turbulence. Unfortunately, this requires rather large Reynolds numbers and is not easy to achieve. However, in a stratified system it is also possible to produce three-dimensional motions by the magnetic buoyancy instability. This was an important agent responsible for driving a dynamo in the model of Cline et al. (2003). Yet another possibility is the magneto-rotational instability, which can also produce three-dimensional motions to drive a dynamo (Brandenburg et al. 1995; Hawley et al. 1996; Stone et al. 1996), but this requires that there is also rotation.

In this paper we investigate a system similar to that of Cline et al. (2003), but with a linear shear profile instead of a sinusoidal one, or rather a modified sinusoidal one where one flank is steeper than the other. Another difference is that

in our model the shear extends through all layers and is not localized near the bottom of the domain, as in the model of Cline et al. (2003). Their setup was motivated by the presence of a strong shear layer in the solar tachocline (Hughes et al. 2007). However, here we are interested in more general aspects rather than particular applications. It is possible that some important dynamics would be lost by ignoring the additional vertical dependence of shear, but this is not well understood at present. Regardless of whether or not self-sustained dynamo action exists, there are a number of issues that deserve to be addressed in such a setup. Firstly, it is useful to determine the energy fluxes between kinetic and magnetic energies and how they are coupled to the shear, for example. Secondly, if magnetic buoyancy plays a role in producing turbulence, it should be possible to quantify this by measuring suitable correlations. In particular, it is not clear whether a stratification that is close to marginally stable is advantageous compared to one that is strongly stable. Finally, in order to assess the possibility of large-scale dynamo action, one needs to determine the turbulent transport coefficients.

2 The model

2.1 Governing equations

We consider a Cartesian domain with externally imposed linear shear and vertical gravity leading to density stratification in the z direction. The full set of hydromagnetic equations for the magnetic vector potential A, the density ρ, the

---

velocity $\boldsymbol{U}$, and the specific internal energy e, can then be written in the form

$$\frac{\mathcal{D}\boldsymbol{A}}{\mathcal{D}t} = -SA_y\hat{\boldsymbol{x}} - (\boldsymbol{\nabla}\boldsymbol{U})^{\mathrm{T}}\boldsymbol{A} - \mu_0\eta\boldsymbol{J}, \tag{1}$$

$$\frac{\mathcal{D}\ln\rho}{\mathcal{D}t} = -\boldsymbol{\nabla}\cdot\boldsymbol{U}, \tag{2}$$

$$\rho\frac{\mathcal{D}\boldsymbol{U}}{\mathcal{D}t} = -S\rho U_x\hat{\boldsymbol{y}} - \boldsymbol{\nabla}p + \rho\boldsymbol{g} + \boldsymbol{J}\times\boldsymbol{B} + \boldsymbol{\nabla}\cdot 2\nu\rho\mathsf{S}, \tag{3}$$

$$\rho\frac{\mathcal{D}e}{\mathcal{D}t} = -p\boldsymbol{\nabla}\cdot\boldsymbol{U} + \boldsymbol{\nabla}\cdot K\boldsymbol{\nabla}T + 2\rho\nu\mathsf{S}^2 + \mu_0\eta\boldsymbol{J}^2, \tag{4}$$

where $\mathcal{D}/\mathcal{D}t = \partial/\partial t + (\boldsymbol{U} + \overline{\boldsymbol{U}}_0)\cdot\boldsymbol{\nabla}$ is the advective derivative, $\overline{\boldsymbol{U}}_0 = (0, Sx, 0)$ is the imposed large-scale shear flow, $\mathsf{S}_{ij} = \frac{1}{2}(U_{i,j} + U_{j,i}) - \frac{1}{3}\delta_{ij}\boldsymbol{\nabla}\cdot\boldsymbol{U}$ is the traceless rate of strain tensor, $\boldsymbol{B} = \boldsymbol{\nabla}\times\boldsymbol{A}$ is the magnetic field, $\boldsymbol{J} = \boldsymbol{\nabla}\times\boldsymbol{B}/\mu_0$ is the current density, μ_0 is the magnetic permeability, η and ν are respectively the magnetic diffusivity and kinematic viscosity, K is the heat conductivity, and $\boldsymbol{g} = -g\hat{\boldsymbol{z}}$ is the gravitational acceleration. The fluid obeys an ideal gas law $p = \rho e(\gamma - 1)$, where p is the pressure, and $\gamma = c_{\mathrm{p}}/c_{\mathrm{v}} = 5/3$ is the ratio of specific heats at constant pressure and volume, respectively. The internal energy per unit mass is related to the temperature via $e = c_{\mathrm{v}}T$.

2.2 Initial and boundary conditions

Our initial stratification is a polytrope where p is proportional to ρ^Γ, and Γ is related to the polytropic index m via $\Gamma = 1 + 1/m$. The superadiabatic gradient is usually defined as the normalized entropy gradient with respect to logarithmic pressure, $\nabla - \nabla_{\mathrm{ad}} = \mathrm{d}(s/c_{\mathrm{p}})/\mathrm{d}\ln p$, i.e.

$$\nabla - \nabla_{\mathrm{ad}} = \gamma^{-1} - \Gamma^{-1}. \tag{5}$$

A stable stratification corresponds to $\nabla - \nabla_{\mathrm{ad}} < 0$, i.e. $\Gamma < \gamma$. Following Cline et al. (2003) we adopt $m = 1.6$, which gives $\nabla - \nabla_{\mathrm{ad}} \approx -0.015$. (We note that the $\nabla - \nabla_{\mathrm{ad}}$ quoted by Cline et al. (2003) is scaled by a factor $2(m+1)$, giving -0.08.)

In a polytrope, the temperature, and hence the square of the sound speed are proportional to the negative gravity potential. Using $c_{\mathrm{s}}^2 = (\gamma - 1)h$ we find

$$c_{\mathrm{s}}^2 = -\frac{\gamma}{m+1}\Phi, \tag{6}$$

where $\Phi = -(z_\infty - z)g$ is the gravitational potential, and the $z_\infty > z$ is the top of the atmosphere where temperature, density and pressure would vanish. In order that $\rho = \rho_0$ and $c_{\mathrm{s}}^2 = c_{\mathrm{s}0}^2$ at a certain reference height $z = -H_0$, we choose

$$z_\infty = -H_0 + (m+1)\frac{c_{\mathrm{s}0}^2}{\gamma g}. \tag{7}$$

We consider a computational domain with horizontal extent $-2 < x/H_0 < 2$, $-2 < y/H_0 < 2$, and vertical extent $-4.12 \leq z/H_0 \leq -1$, where $z/H_0 = -1$ corresponds to the top of the layer.

Our initial magnetic field is given by a flux tube pointing in the x direction, but with a perturbation in the x direction. Thus, our vector potential is given by

$$\boldsymbol{A} = B_0\frac{1 + \epsilon\cos k_x x}{1 + \delta\boldsymbol{r}^2/R^2}\hat{\boldsymbol{x}}\times\delta\boldsymbol{r}, \tag{8}$$

where $\delta\boldsymbol{r} = (x, y, z - z_0)$ is the distance from the core of the tube in the yz plane. We choose $B_0 = 0.1\sqrt{gH_0\rho_0\mu_0}$, $\epsilon = 0.3$, $R = 0.2H_0$, and $z_0 = -3H_0$.

In all cases we use stress-free boundary conditions for the velocity,

$$U_{x,z} = U_{y,z} = U_z = 0, \tag{9}$$

together with a vertical field condition, i.e.

$$B_x = B_y = 0. \tag{10}$$

For the specific entropy we use either an extrapolating boundary condition, which allows the values of thermodynamic variables on the two boundaries to change freely (Run A), or we fix the energy influx at the bottom and the temperature at the top (Run B). The latter condition is also used by Cline et al. (2003).

2.3 Units and control parameters

Non-dimensional quantities are obtained by setting

$$d = g = \rho_0 = c_{\mathrm{p}} = \mu_0 = 1, \tag{11}$$

where ρ_0 is the initial density at z_{top}. The units of length, time, velocity, density, entropy, and magnetic field are

$$\begin{aligned}&[x] = H_0, \quad [t] = \sqrt{H_0/g}, \quad [U] = \sqrt{gH_0}, \quad [\rho] = \rho_0, \\ &[s] = c_{\mathrm{p}}, \quad [B] = \sqrt{gH_0\rho_0\mu_0}.\end{aligned} \tag{12}$$

We define the fluid and magnetic Prandtl numbers as

$$\mathrm{Pr} = \frac{\nu}{\chi_0}, \quad P_{\mathrm{m}} = \frac{\nu}{\eta}, \tag{13}$$

where $\chi_0 = K/(\rho_{\mathrm{m}}c_{\mathrm{p}})$ is the thermal diffusivity, and ρ_0 is the density at $z = -H_0$. We define the magnetic Reynolds number and the shear parameter via

$$\mathrm{Rm} = \frac{u_{\mathrm{rms}}}{\eta k_{\mathrm{f}}}, \quad \mathrm{Sh} = \frac{S}{u_{\mathrm{rms}}k_{\mathrm{f}}}, \tag{14}$$

where $k_{\mathrm{f}} = 2\pi/H_0$ is assumed as a reasonable estimate for the wavenumber of the energy-carrying eddies.

The simulations were performed with the PENCIL CODE[1], which uses sixth-order explicit finite differences in space and third order accurate time stepping method. The dependent variables are $\boldsymbol{A}$, $\ln\rho$, $\boldsymbol{U}$, and the specific entropy s, which is related to the speed of sound c_{s} via

$$c_{\mathrm{s}}^2 = c_{\mathrm{s}0}^2[(\gamma - 1)\ln(\rho/\rho_0) + \gamma s/c_{\mathrm{p}}], \tag{15}$$

where $c_{\mathrm{s}0}$ and ρ_0 are normalization constants.

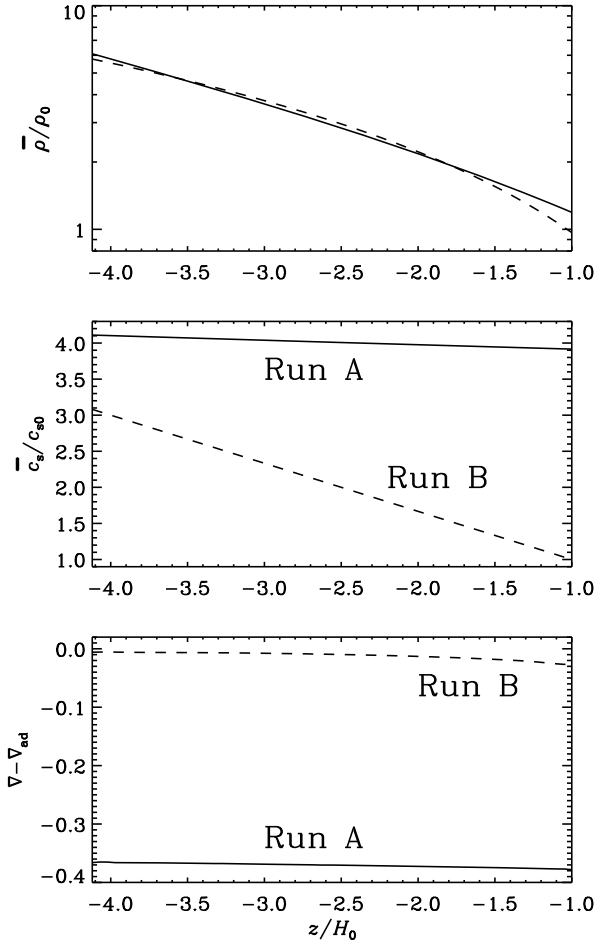---

[1] http://www.nordita.org/software/pencil-code/

Fig. 1 Final stratification for Runs A (solid lines) and B (dashed lines). Note that Run A is nearly isothermal (constant sound speed c_s) while Run B is nearly isentropic ($\nabla - \nabla_{ad}$ is close to zero).

3 General features of the simulation results

In the following we discuss Runs A and B that differ only in the boundary conditions adopted for the entropy. For Run A we use extrapolating boundary conditions for the specific entropy, while for Run B we fix the energy influx at the bottom and the temperature at the top. In all cases we use the same polytropic initial condition.

We have evolved both simulations for several thermal and magnetic diffusion times. The mean stratification settles then to a new stratification (Fig. 1). Runs A and B differ mainly in the mean temperature gradient which becomes nearly constant in Run A and stays finite for Run B. For Run B we find that $\nabla - \nabla_{ad} \approx -0.01$; see Fig. 1, so it is stably stratified, but close to marginal. By contrast, in Run B the stratification is strongly stable with $\nabla - \nabla_{ad} \approx -0.38$.

When the simulation is started the initial flux tube begins to rise owing to magnetic buoyancy, and it is also being sheared out in the streamwise direction. Both effects can clearly be seen in a tz diagram of $\overline{B}_x$ and $\overline{B}_y$; see Fig. 2. Unless noted otherwise, an overbar denotes averaging over the x and y directions. The initial phase of the buoyant rise
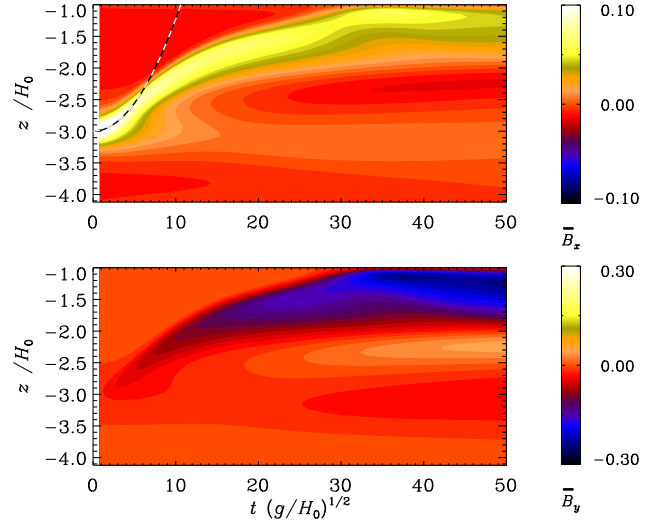

Fig. 2 (online colour at: www.an-journal.org) Visualization of $\overline{B}_x$ and $\overline{B}_y$ as functions of t and z for Run A. Note the initial ascent of $\overline{B}_x$ as well as the subsequent amplification of $\overline{B}_y$. For comparison, the curve $z = \frac{1}{2}(\delta\rho/\rho)gt^2 - z_0$ has been overplotted with an estimated value of $\delta\rho/\rho = 0.2$.

follows approximately a parabolic trajectory, as is indicated by the superimposed dashed line in the first panel.

The effects of magnetic buoyancy can also be established at later times through a systematic correlation between strong fields and upward motion. We define a normalized buoyancy parameter,

$$\mathrm{Bu} = \langle (\rho U_z)' \boldsymbol{B}^2 \rangle / (\rho_0 U_{\mathrm{rms}} B_{\mathrm{rms}}^2), \tag{16}$$

where the dash in $(\rho U_z)'$ denotes the departure of the mass flux from the horizontal mean. It turns out that Bu is always positive. This means that strong fields are systematically correlated with upward motions and vice versa. For Run A this value is ≈ 0.035 and for Run B it is ≈ 0.07. This supports the idea that magnetic buoyancy is indeed active, but it is not clear that it still plays an important role at late times compared to early times. The peak values of Bu are around 3.5 at $t \approx 5(g/H_0)^{1/2}$ both for Runs A and B.

In Figs. 3 and 4 we show the values of U_z and B_z on the periphery of the computational domain for Runs A and B at different times. Toward the end of the simulation the state appears nearly perfectly steady, but there are actually persistent low amplitude oscillations that remain excited at all times. In Fig. 5 we show a zt diagram of the mean vertical velocity, $\overline{U}_z$. The frequency of these oscillations is about $0.9\,(g/H_0)^{1/2}$, This value lies between that of the Brunt-Väisälä frequency, whose local value varies between 0.4 and 0.5 from bottom to top of the domain, and the acoustic frequency of about $2\,(g/H_0)^{1/2}$. Alfvén oscillations are also possible; their frequency is about 0.2 for Run A in the final state.

In Fig. 6 we plot the evolution of U_{rms} and B_{rms} in diffusive time units, expressed in terms of the magnetic Reynolds number $R_m = U_{\mathrm{rms}}/\eta k_1$ and Lundquist
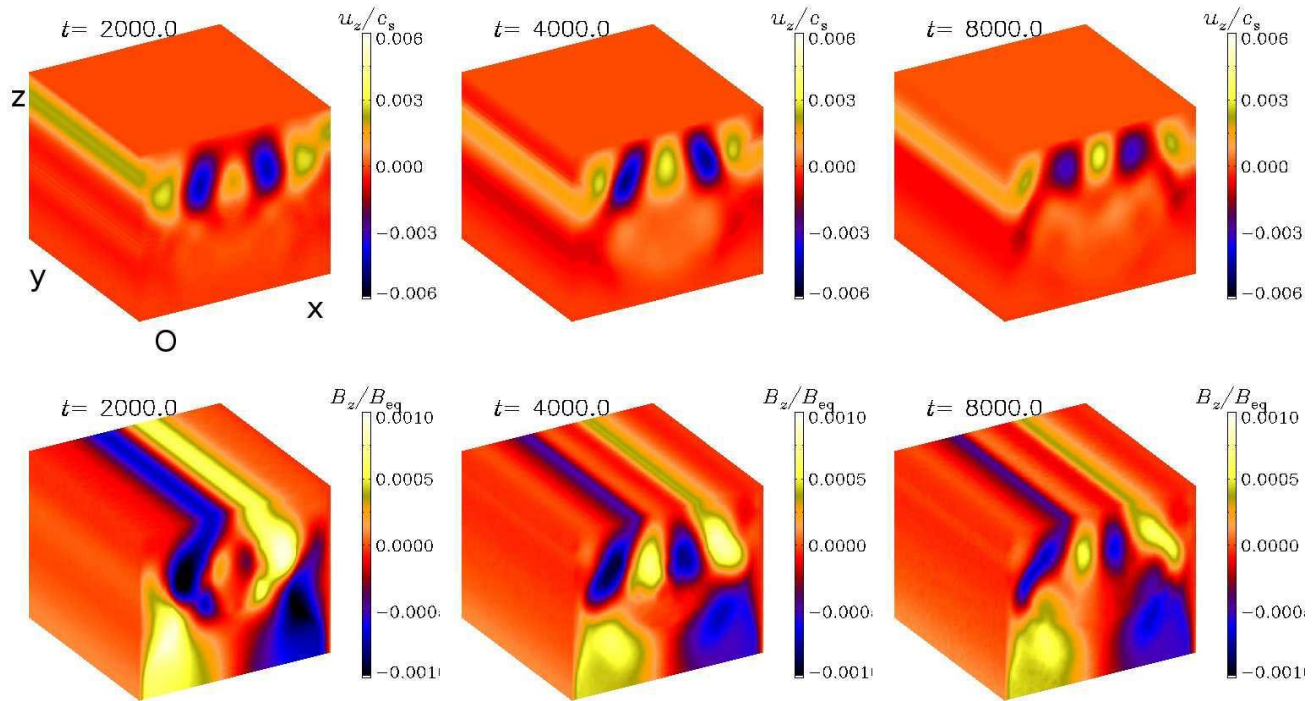
Fig. 3 (online colour at: www.an-journal.org) Visualization of U_z (*upper row*) and B_z (*lower row*) for Run A at different times. The coordinate directions are indicated in the upper left panel. Note the symmetry of U_z and the antisymmetry of B_z with respect to $x = 0$.
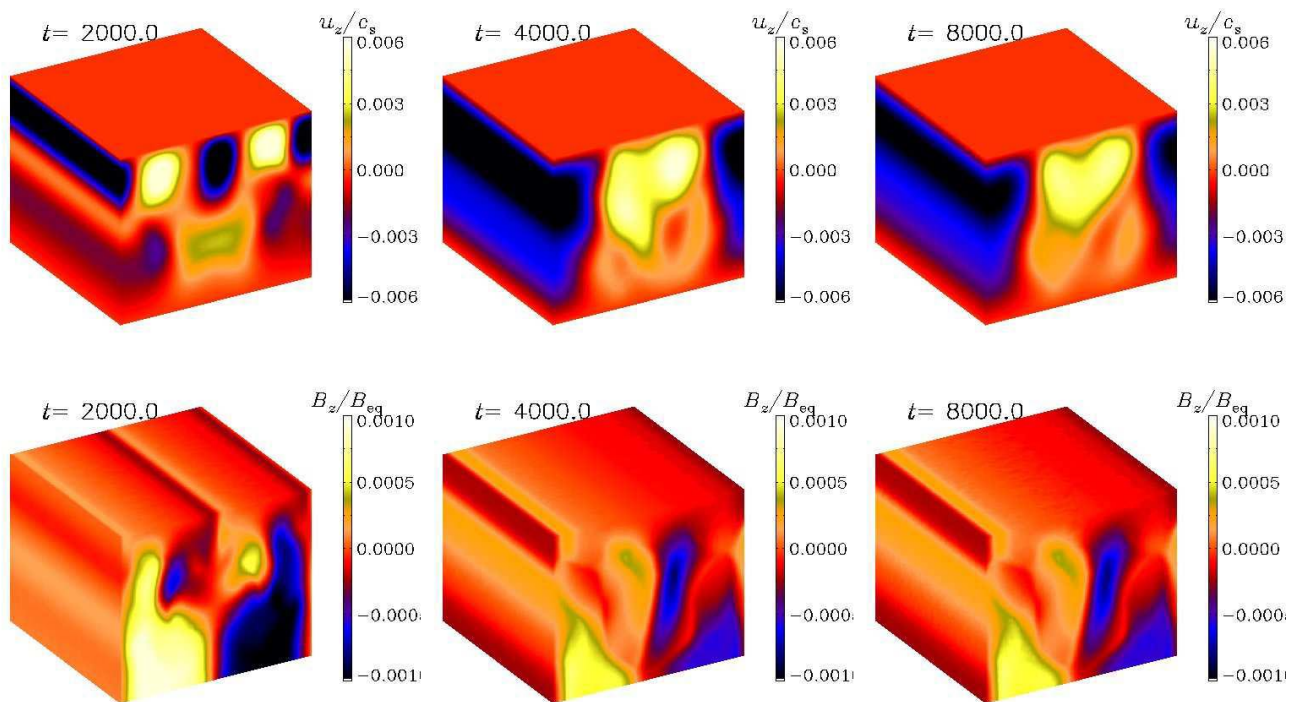

Fig. 4 (online colour at: www.an-journal.org) Same as Fig. 3, but for Run B. Here both U_z and B_z have no symmetry property with respect to $x = 0$.
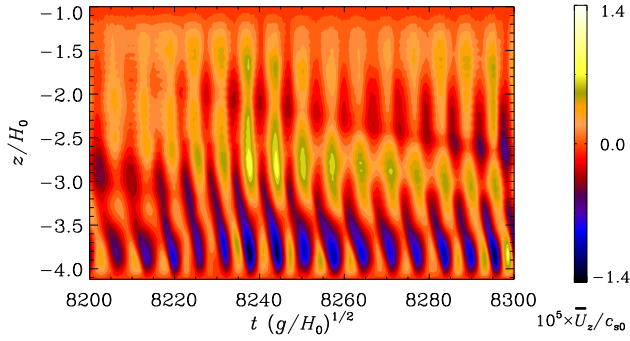
Fig. 5 (online colour at: www.an-journal.org) Horizontally averaged mean vertical velocity showing persistent low amplitude oscillations for Run A at late times after $t = 8200 \, (H_0/g)^{1/2}$.
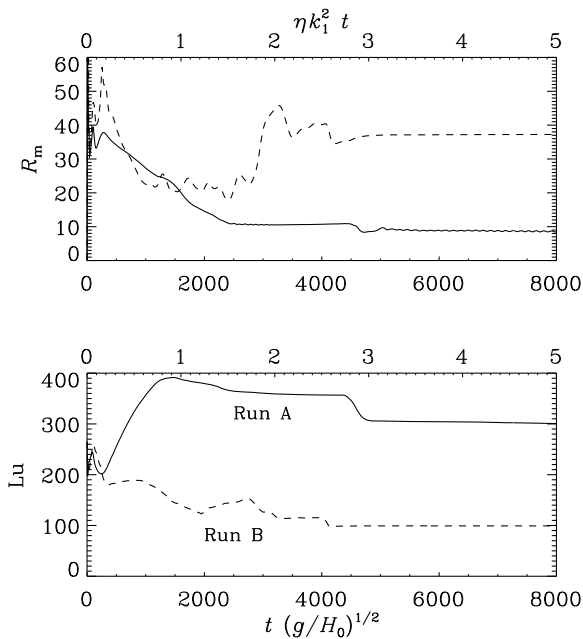

Fig. 6 Comparison of the evolution of rms velocity and magnetic field, normalized in resistive units and expressed in terms of R_{m} and Lu, for Runs A and B. The lower abscissa give time in dynamical units and the upper one in resistive units.

number Lu $= v_{\mathrm{A,rms}}/\eta k_1$, respectively. Here, $v_{\mathrm{A,rms}} = B_{\mathrm{rms}}/\sqrt{\mu_0\rho 0}$ is the Alfvén speed. Note that toward the end of the simulation we have $R_{\mathrm{m}} \approx 10$ and Lu ≈ 300. There is no evident tendency for decay.

4 Flow of energy

In order to understand where the energy comes from we consider here the energetics of the system. In a stratified hydromagnetic system there are four forms of energy: potential, kinetic, thermal, and magnetic energy, defined respectively by

$$E_{\mathrm{P}} = \int \rho\phi \, \mathrm{d}V, \quad E_{\mathrm{K}} = \int \tfrac{1}{2}\rho U^2 \, \mathrm{d}V, \tag{17}$$
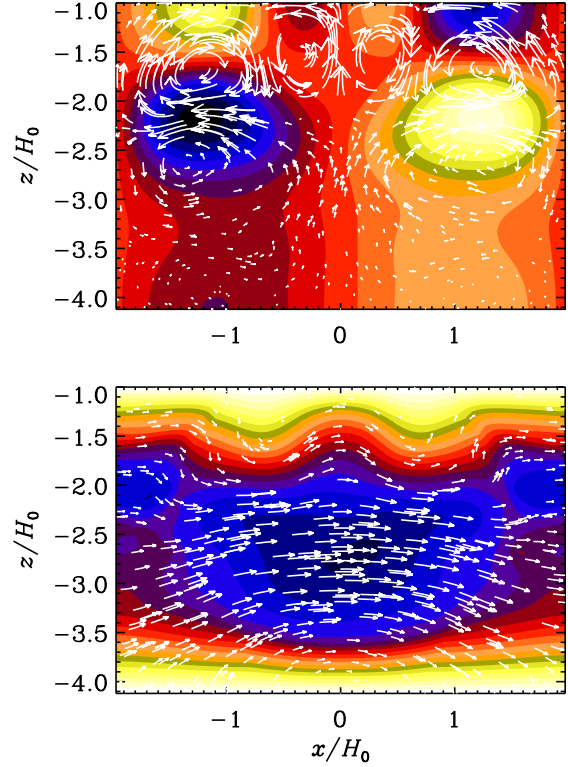

Fig. 7 (online colour at: www.an-journal.org) Zonally averaged velocity (upper panel) and magnetic field vectors (lower panel) in the xz plane superimposed on the corresponding y components of these fields for Run A in the final and nearly steady state. Note the presence of a mean field with $\overline{B}_x > 0$ and $\overline{B}_y < 0$, so $\overline{B}_x\overline{B}_y < 0$, as expected for negative shear.

$$E_{\mathrm{T}} = \int \rho e \, \mathrm{d}V, \quad E_{\mathrm{M}} = \int \tfrac{1}{2\mu_0}\boldsymbol{B}^2 \, \mathrm{d}V. \tag{18}$$

In the presence of stress-free boundary conditions, the evolution of these energies is governed by the following four ordinary differential equations:

$$\dot{\mathrm{E}}_{\mathrm{P}} + W_{\mathrm{b}} = 0, \tag{19}$$

$$\dot{\mathrm{E}}_{\mathrm{K}} - W_{\mathrm{b}} - W_{\mathrm{c}} - W_{\mathrm{L}} - \epsilon_{\mathrm{K}}^{\mathrm{S}} + \epsilon_{\mathrm{K}} = 0, \tag{20}$$

$$\dot{\mathrm{E}}_{\mathrm{T}} + W_{\mathrm{c}} - \epsilon_{\mathrm{K}} - \epsilon_{\mathrm{M}} - L_{\mathrm{bot}} + L_{\mathrm{top}} = 0, \tag{21}$$

$$\dot{\mathrm{E}}_{\mathrm{M}} + W_{\mathrm{L}} - \epsilon_{\mathrm{M}}^{\mathrm{S}} + \epsilon_{\mathrm{M}} = 0, \tag{22}$$

where dots denote time derivatives,

$$W_{\mathrm{b}} = \int \rho \boldsymbol{U} \cdot \boldsymbol{g} \, \mathrm{d}V, \quad W_{\mathrm{c}} = \int p \boldsymbol{\nabla} \cdot \boldsymbol{U} \, \mathrm{d}V, \tag{23}$$

describe the work done by buoyancy and compression,

$$W_{\mathrm{L}} = \int \boldsymbol{U} \cdot (\boldsymbol{J} \times \boldsymbol{B}) \, \mathrm{d}V, \tag{24}$$

is the work done by the Lorentz force,

$$\epsilon_{\mathrm{K}}^{\mathrm{S}} = -\int \rho \boldsymbol{U}(\mathbf{S}\boldsymbol{U}) \, \mathrm{d}V, \quad \epsilon_{\mathrm{M}}^{\mathrm{S}} = \int \mu_0^{-1}\boldsymbol{B}(\mathbf{S}\boldsymbol{B}) \, \mathrm{d}V, \tag{25}$$

couple shear to kinetic and magnetic energy reservoirs,

$$\epsilon_{\mathrm{K}} = \int 2\rho\nu\mathbf{S}^2 \, \mathrm{d}V, \quad \epsilon_{\mathrm{M}} = \int \sigma^{-1}\boldsymbol{J}^2 \, \mathrm{d}V, \tag{26}$$
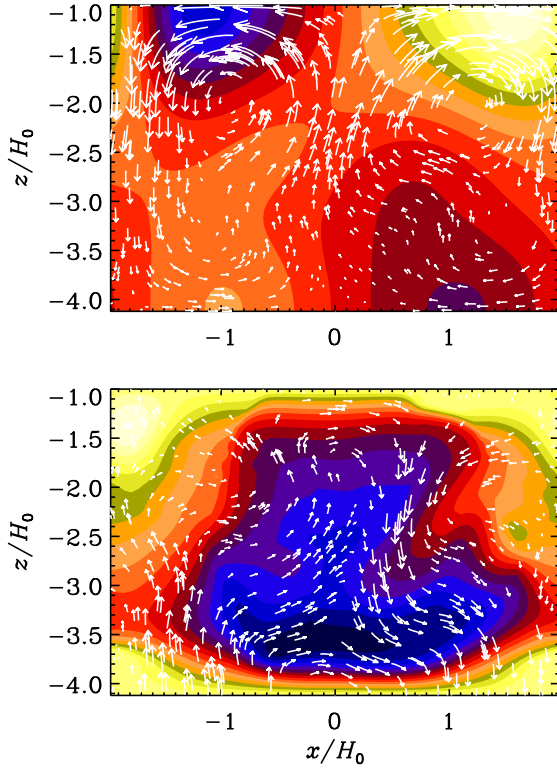
Fig. 8 (online colour at: www.an-journal.org) Same as Fig. 7, but for Run B.

are viscous and Joule dissipation, and

$$L_{\text{top}} = \int_{\text{top}} \boldsymbol{F}_{\text{R}} \cdot \mathrm{d}\boldsymbol{S}, \quad L_{\text{bot}} = \int_{\text{bot}} \boldsymbol{F}_{\text{R}} \cdot \mathrm{d}\boldsymbol{S}, \qquad (27)$$

are the luminosities at top and bottom of the domain. The evolution of total energy, $E_{\text{tot}} = E_{\text{P}} + E_{\text{K}} + E_{\text{T}} + E_{\text{M}}$, is therefore governed by

$$\dot{E}_{\text{tot}} = \epsilon_{\text{K}}^{\text{S}} + \epsilon_{\text{M}}^{\text{S}} + L_{\text{bot}} - L_{\text{top}}, \qquad (28)$$

i.e. energy is supplied by shear coupling to kinetic and magnetic energies, as well as by heating from below, and energy is removed by radiation at the top.

Energy is exchanged and transformed into other types of energy, as is shown in Figs. 10 and 11 for Runs A and B, respectively. It should be noted that, even if the system is not perfectly in a steady state, we cannot expect perfect energy balance, because the code solves the equations in non-conservative form. However, the discrepancies should become smaller at larger numerical resolution. We notice that in all cases the energy flux at the top of the domain is less than at the bottom, and that these values are much larger than any of the other energy fluxes in the system. This is related to the discretization error of the scheme and does not indicate that energy is taken from the thermal energy flux. For Run B there is another obvious problem in that the magnetic energy dissipation is much larger than what can be accounted for by the influx of energy by shear. This is related to the fact that in this run there is a fairly strong magnetic field whose maintenance may be explained purely
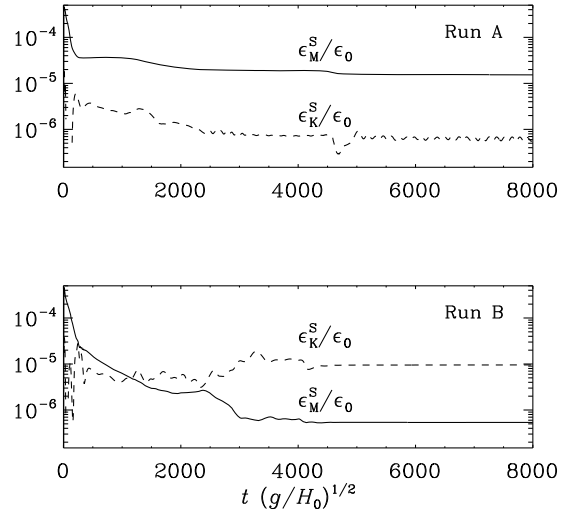

Fig. 9 Plot of the energy input from shear via the terms $\epsilon_{\text{K}}^{\text{S}}$ and $\epsilon_{\text{M}}^{\text{S}}$. Note the larger excess of $\epsilon_{\text{M}}^{\text{S}}$ compared with $\epsilon_{\text{K}}^{\text{S}}$ for Run A compared with Run B.
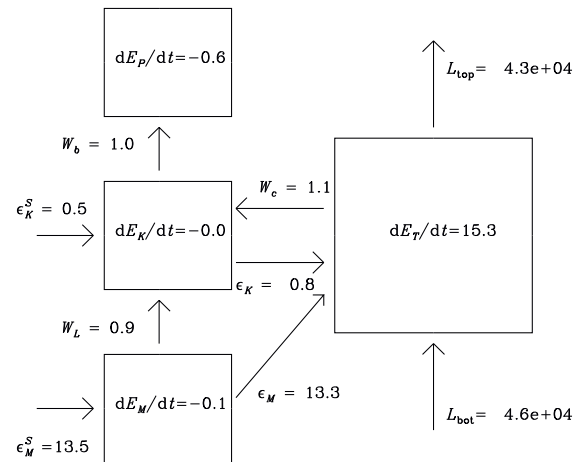

Fig. 10 Flow diagram showing the conversion between different energy forms for Run A. All energy fluxes are normalized with respect to the averaged magnetic energy content times the modulus of the shear rate and multiplied by a factor of 1000 to bring the values closer to unity.

as the result of numerical errors, even though no obvious problems can be seen from images such as Figs. 3 and 4. This could be related to the fact that there are low amplitude azimuthal variations with a relative amplitude of about 10^{-5} that cannot be seen unless the mean field is subtracted out. In any case, we should keep in mind that the reason for the maintenance of magnetic energy could be related to a very weak "non-axisymmetry" of the field that is related to numerical noise. Regardless of these subtle shortcomings, there are many aspects that do make sense. In particular in Run A the balance between inflow and outflow of magnetic energy is quite reasonable, and so is the balance of kinetic
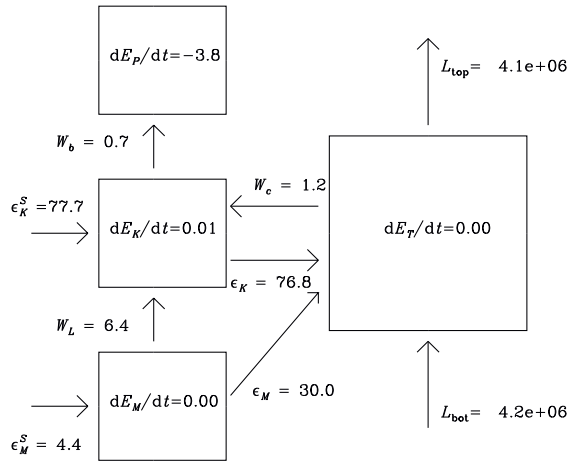
Fig. 11   Same as Fig. 10, but for Run B.

Fig. 12 $\overline{B}_y$ (solid line) together with $100 \times \overline{B}_x$ (*upper panel*) and $\overline{U}_y$ (solid line) together with $10 \times \overline{U}_x$ and $10 \times \overline{U}_z$ (*lower panel*), for Run A, time averaged over the last 1000 time units.

energy in Run B. This suggests that the flows in Run A are mainly driven by work done by the magnetic field against the shear, while in Run B the driving comes mostly from work done by the Reynolds stress against the shear.

5   Profiles of mean field and velocity

It is interesting to confront the mean profile of the magnetic field with stability criteria for magnetic buoyancy instabilities. Following Newcomb (1961), a necessary condition for instability is

$$\mathrm{d}\ln|\boldsymbol{B}|/\mathrm{d}z > \gamma H_p N^2/v_A^2 \qquad (29)$$

(see also Hughes & Proctor 1988). This condition is actually met in the upper quarter of the simulation domain where there is a rapid decrease of $|\boldsymbol{B}|$ with height; see the top panel of Fig. 12 for Run A.

The mean "toroidal" velocity, $\overline{U}_y$ shows a systematic variation in the z direction that is reminiscent of that found for isotropically forced shear-flow turbulence (Käpylä et al. 2009), which was then interpreted in terms of a vorticity dynamo (Elperin et al. 2003). In the present case, however, the magnetic field is already so strong that such an effect would be suppressed. Therefore, the flow is here more like a direct response to the magnetic field. The other two components of the mean flow are negligible by comparison. However, we recall that the z component of the mean velocity shows persistent low amplitude oscillations (Fig. 5) that are not present in the other two components.

6   Mean-field transport coefficients

In order to characterize the flow properties further we now consider the ability of the flow to mix and to produce large-scale magnetic fields. We do this by using the test-field method of Schrinner et al. (2005, 2007) with sinusoidal test fields, as explained in detail in Brandenburg (2005) and
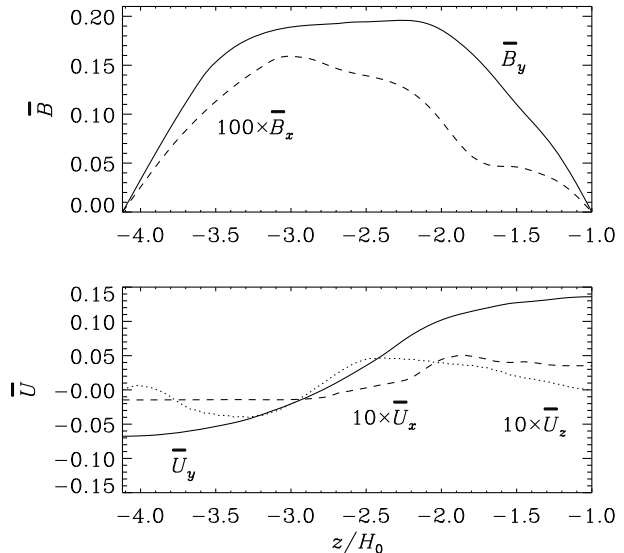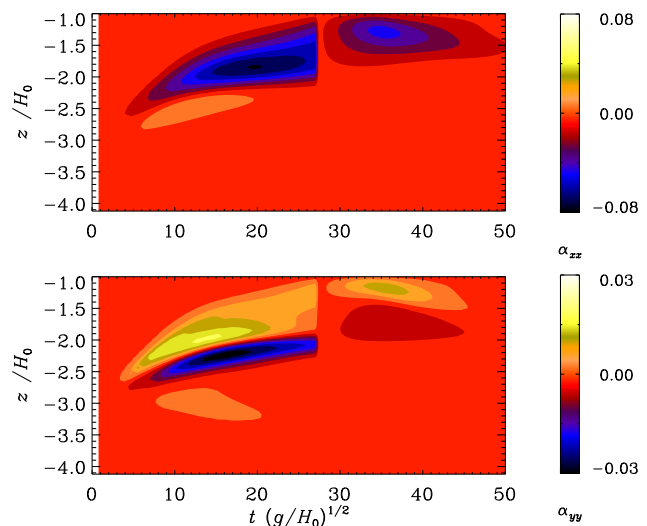

Fig. 13   (online colour at: www.an-journal.org) Diagonal component of the α tensor for Run A at early times (*upper panel* is for α_{xx} and *lower panel* for α_{yy}). Note that α_{yy} is negative in the lower part of the initial rising flux tube and positive above, while α_{xx} is negative throughout.

Brandenburg et al. (2008a,b). In Fig. 13 we plot α_{xx} and α_{yy} versus time and height for Run A at early times. It turns out that α_{xx} is mainly negative at the location of the initial rising flux tube while α_{yy} is negative in the lower part of the tube and positive above. In order to interpret this result we compare now with expectations from mean-field theory.

The combined presence of shear and magnetic buoyancy is particularly interesting, because one may expect there to be an additional contribution that is related to the magnetic stress, $\overline{b_x b_y}$ (Brandenburg 1998). Such behavior was also re-
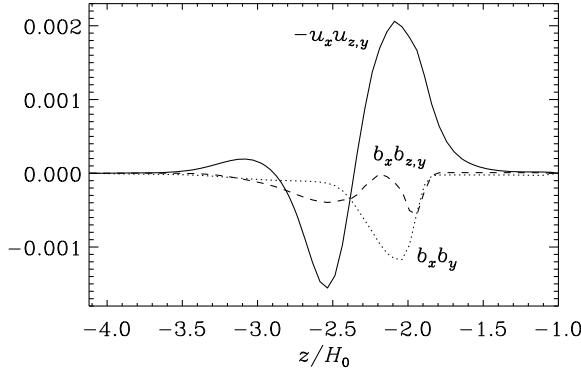
Fig. 14 Vertical profiles of $-\overline{u_x u_{z,y}}/g$ (solid line), $\overline{b_x b_{z,y}}/g(\mu_0 \rho_0)^{1/2}$ (dashed line), and $\epsilon_{\mathrm{buoy}} \times \overline{b_x b_y}/c_s^2(\mu_0 \rho_0)^{1/2}$ with $\epsilon_{\mathrm{buoy}} = 0.1$ (dotted line) for Run A at $t = 10(H_0/g)^{1/2}$.

produced using the second order correlation approximation (Rüdiger & Pipin 2000). In the spirit of the τ approximation (e.g. Blackman & Field 2003) this term can be derived by calculating $\partial\overline{\mathcal{E}}/\partial t$, which has contributions from $\overline{u \times \dot{b}}$ and $\overline{\dot{u} \times b}$. The first term, which gives rise to the usual kinetic α effect, is

$$\overline{(u \times \dot{b})}_y = \overline{B}_y \overline{u_{z,y} u_x} + ...,\qquad(30)$$

while the second term, which gives rise to the magnetic α effect as well as a new term proportional to $\overline{b_x b_y}$. To derive the second term we consider here the momentum equation in the form

$$\dot{u} = ... + \overline{B} \cdot b/\rho\mu_0 + \frac{\delta\rho}{\rho}g,\qquad(31)$$

where dots refer to additional terms that are less relevant for the present discussion. Replacing $\delta\rho/\rho$ by $B^2/2p\mu_0$ and linearizing about $\overline{B}_y$, i.e. $\delta\rho/\rho \approx -\overline{B}_y b_y/p\mu_0$, yields

$$\overline{(\dot{u} \times b)}_y = \overline{B}_y \left(\overline{b_{z,y} b_x}/\rho\mu_0 + g\overline{b_y b_x}/\mu_0 p\right) + ...\qquad(32)$$

Therefore the yy component of α should be

$$\alpha_{yy} = -\tau\overline{u_x u_{z,y}} + \frac{\tau}{\mu_0\rho}\left(\overline{b_x b_{z,y}} + \epsilon_{\mathrm{buoy}}\overline{b_x b_y}/H_0\right) + ...,\qquad(33)$$

where ϵ_{buoy} is an empirical non-dimensional parameter quantifying the relative importance of magnetic buoyancy effects. In Fig. 14 we plot the contributions from all three terms for Run A at $t = 10(H_0/g)^{1/2}$. It turns out that the main part of the vertical variation of α_{yy} is not determined by magnetic and buoyancy effects, but rather by the kinematic contribution proportional to $-\overline{u_x u_{z,y}}$.

The maintenance of the magnetic field over resistive time scales can only be explained if there is a mean electromotive in the y direction that can balance the resistive losses of $\overline{B}_x$. Those losses are proportional to $\eta\partial\overline{B}_x/\partial z$, which gives the main contribution to $\overline{J}_y$, that is proportional to $\overline{\mathcal{E}}_y(z)$. This is clearly suspicious and suggests that the fluctuations in the y direction are insufficient to explain the observed mean magnetic field. This result is also in agreement
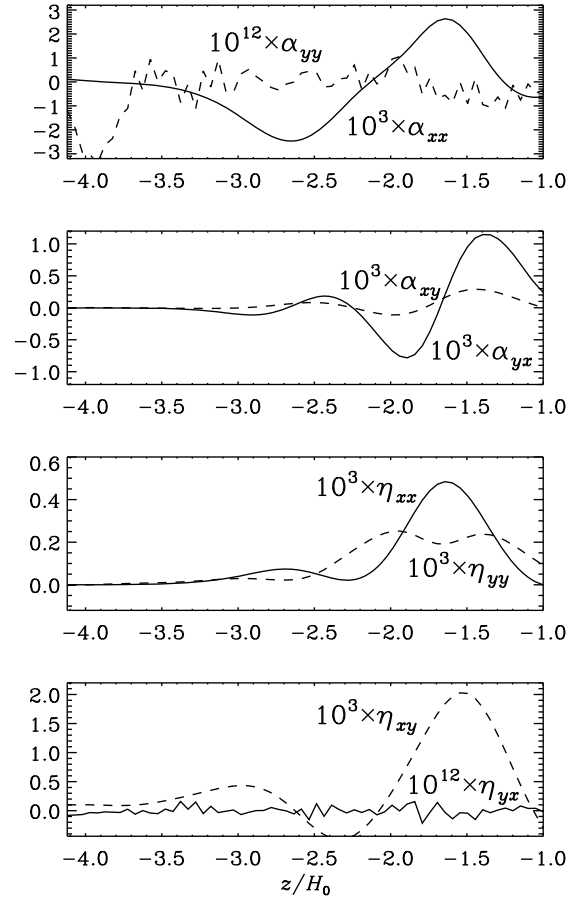

Fig. 15 All components of the α and η tensors near the end of the run for Run A. Note that α_{yy} and η_{yx} are at the noise level and have been multiplied by large factors ($\times 10^{12}$) to see at least the noise.

with the fact that α_{yy} and η_{xy}, are found to be essentially around zero (Fig. 15). Thus, with the present knowledge we cannot propose a physical mechanism for the maintenance of the observed mean field.

In Fig. 16 (upper row) we plot $\overline{\mathcal{E}}_y(z)$ and confirm that it is large enough to balance $\eta\partial\overline{B}_x/\partial z$, which is overplotted by a dashed line. The two curves are not in perfect agreement, but this could partly be explained by the fact that the mean field is time-dependent and shows persistent low-amplitude oscillations. However, there is a caveat in that the definition of the fluctuating quantities, u and b that enter $\overline{\mathcal{E}} = \overline{u \times b}$, have been computed using xy averages. If we use only y averages, so that the mean field depends on both x and y, we find values that are essentially compatible with zero (see the lower row of Fig. 16). Also the strength of fluctuations is rather low in that case.

7 Conclusions

In an attempt to study the possibility of dynamo action mediated by magnetic buoyancy and driven by work done against an externally imposed linear shear we came across a
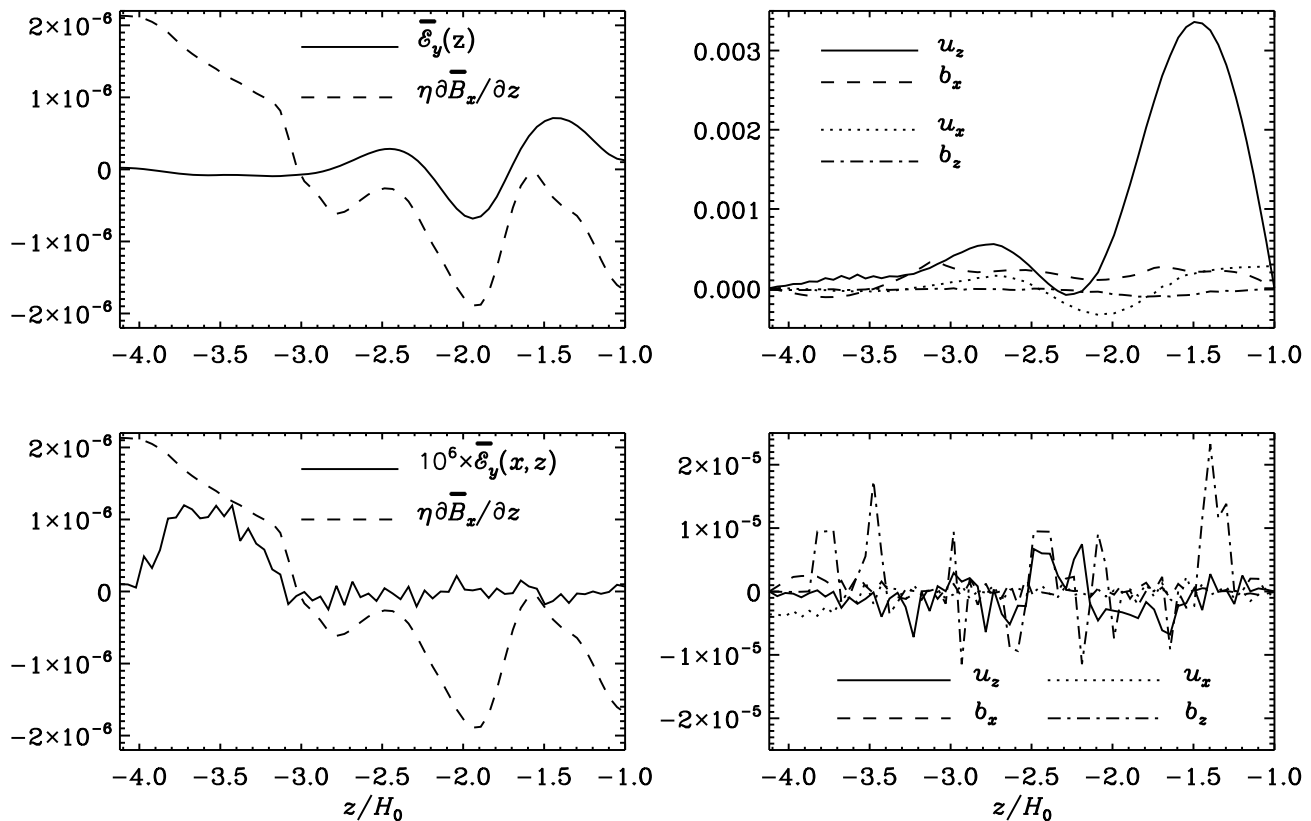
Fig. 16 Mean electromotive force in the y direction overplotted with the corresponding resistive losses (*left panels*) together with plots showing the z dependence of u_z and b_x as well as u_x and b_z for Run A. For the upper row xy averages were used while for the lower row just y averages have been employed.

number of unusual phenomena. Most surprising is probably the build-up and apparent maintenance of a strong magnetic field. The ratio of the Alfvén speed to the sound speed is about 0.1, while the ratio of the Alfvén speed to the rms velocity of the motions is about 10. The magnetic field is nearly axisymmetric, i.e. independent of y. In view of Cowling's theorem, this clearly raises doubts about the validity of this result. The possibility of numerical problems is supported by the fact that at least for Run B there is an unexplained imbalance between magnetic energy input and output. On the other hand, this rather obvious imbalance applies only to Run B, which is nearly isentropic. For Run A the overall energy balance is better. Also, there are no obvious deficiencies that one would normally expect in the case of insufficient numerical resolution such as oscillations on the grid scale.

An important clue might be that the magnitude of the mean magnetic field in the cross-stream direction can only be explained if the $\overline{\boldsymbol{u} \times \boldsymbol{b}}$ correlation of the fluctuations are evaluated as the departures from a horizontal xy average. If one takes just toroidal or y averages, the resulting correlation drops by six orders of magnitude into the numerical noise. In this context it should be noted that our calculations are normally performed in single precision, which has been

sufficient for most previous applications. The present simulations may present an exception to this.

Yet another possible clue comes from the fact that our models exhibit sustained oscillations. They are most prominent in the isothermal case (Run A) and less prominent in the nearly isentropic case (Run B). This may suggest that buoyancy oscillations could contribute to driving the mean electromotive force responsible for sustaining the mean field $\overline{B}_x$ in the cross-stream direction. (The mean field in the streamwise direction, $\overline{B}_y$, is readily explained by the shear.) On the other hand, an analysis of the flow in terms of the test-field method reveals that both α_{yy} and η_{yx} are essentially zero in the final state, making it impossible to explain the magnetic field as a result of an α effect or a shear–current effect.

In any case, it is clear that shear-driven flows in stratified systems can exhibit rich behavior. Magnetic buoyancy effects are clearly seen at early times shortly after injecting the initial cross-stream magnetic field. Within the present setup we have not seen the vigorous dynamo action with visibly nonaxisymmetric fields reported by Cline et al. (2003). This could simply be related to differences in the parameters or to differences in the flow geometry. We recall that in Cline et al. (2003) there was a non-shearing upper part that is absent in the present work. In addition, they used a peri-

odic shear profile rather than a linear one. In any case, it will be worthwhile performing new simulations using perhaps also other methods and certainly larger resolution. It may be worthwhile to continue these studies using an isothermal setup rather than a nearly isentropic one, provided the oscillations seen in the present work are indeed an important element of the overall dynamics.

References

Blackman, E.G., Field, G.B.: 2003, PhFl 15, L73

Brandenburg, A.: 2005, AN 326, 787

Brandenburg, A.: 1998, in: M.A. Abramowicz, G. Björnsson, J.E. Pringle (eds.), *Theory of Black Hole Accretion Discs*, p. 61

Brandenburg, A., Nordlund, Å., Stein, R.F., Torkelsson, U.: 1995, ApJ 446, 741

Brandenburg, A., Rädler, K.-H., Schrinner, M.: 2008a, A&A 482, 739

Brandenburg, A., Rädler, K.-H., Rheinhardt, M., Käpylä, P.J.: 2008b, ApJ 676, 740

Cline, K.S., Brummell, N.H., Cattaneo, F.: 2003, ApJ 599, 1449

Cowling, T.G.: 1933, MNRAS 94, 39

Elperin, T., Kleeorin, N., Rogachevskii, I.: 2003, Phys Rev E 68, 016311

Hawley, J.F., Gammie, C.F., Balbus, S.A.: 1996, ApJ 464, 690

Hughes, D.W., Proctor, M.R.E.: 1988, AnRFM 20, 187

Hughes, D.W., Rosner, R., Weiss, N.O.: 2007, *The Solar Tachocline*, Cambridge University Press, Cambridge

Käpylä, P.J., Mitra, D., Brandenburg, A.: 2009, Phys Rev E 79, 016302

Newcomb, W.A.: 1961, PhFl 4, 391

Rüdiger, G., Pipin, V.V.: 2000, A&A 362, 756

Schrinner, M., Rädler, K.-H., Schmitt, D., Rheinhardt, M., Christensen, U.: 2005, AN 326, 245

Schrinner, M., Rädler, K.-H., Schmitt, D., Rheinhardt, M., Christensen, U.R.: 2007, GApFD 101, 81

Stone, J.M., Hawley, J.F., Gammie, C.F., Balbus, S.A.: 1996, ApJ 463, 656